# Deep Learning-Based Development of Personalized Human Head Model With Non-Uniform Conductivity for Brain Stimulation

Essam A. Rashed, *Senior Member, IEEE*, Jose Gomez-Tames, *Member, IEEE*, and Akimasa Hirata, *Fellow, IEEE*

***Abstract*— Electromagnetic stimulation of the human brain is a key tool for neurophysiological characterization and the diagnosis of several neurological disorders. Transcranial magnetic stimulation (TMS) is a commonly used clinical procedure. However, personalized TMS requires a pipeline for individual head model generation to provide target-specific stimulation. This process includes intensive segmentation of several head tissues based on magnetic resonance imaging (MRI), which has significant potential for segmentation error, especially for low-contrast tissues. Additionally, a uniform electrical conductivity is assigned to each tissue in the model, which is an unrealistic assumption based on conventional volume conductor modeling. This study proposes a novel approach for fast and automatic estimation of the electric conductivity in the human head for volume conductor models without anatomical segmentation. A convolutional neural network is designed to estimate personalized electrical conductivity values based on anatomical information obtained from T1- and T2-weighted MRI scans. This approach can avoid the time-consuming process of tissue segmentation and maximize the advantages of position-dependent conductivity assignment based on the water content values estimated from MRI intensity values. The computational results of the proposed approach provide similar but smoother electric field distributions of the brain than that provided by conventional approaches.**

***Index Terms*— Precision medicine, electrical conductivity, MRI, deep learning, convolutional neural networks, TMS.**

## I. Introduction

IN ELECTROMAGNETIC dosimetry applications, the use of computational models that imitate human anatomy is an essential process [1]. Such models are used to simulate biological tissues as volume conductors for electromagnetic characterization and neuromodulation applications, as well as for human safety studies. A current major trend in healthcare services is precision medicine, where medical decisions, treatments, or diagnoses are customized to fit the characteristics and conditions of individual subjects.

The recent developments in medical imaging have led to the availability of more personalized data for precision medicine applications related to brain disorders [2], [3]. For the electromagnetic stimulation of the brain, the development of personalized head models is an emerging trend with the goal of avoiding the significant inconsistency caused by inter- and intra-subject variability [4]. The current standard pipeline for human head modeling begins with the acquisition of anatomical images (magnetic resonance imaging (MRI) or computed tomography (CT)), followed by intensive segmentation of different tissue compositions [5]. Therefore, a uniform tissue conductivity is assigned to each annotated tissue (Fig. 1). In most cases, an isotropic conductivity is assumed to be valid for almost all structures. This approach has several limitations that could lead to inappropriate estimation of *in situ* electric fields, thereby reducing the accuracy of stimulation planning. First, the human head is known to be composed of different biological tissues with a wide range of conductivity values [6]. Some of these tissues, especially non-brain tissues, exhibit low contrast or only appear within limited regions in anatomical images. Therefore, the segmentation of all tissues is a challenging task, which is difficult to perform with high quality for all tissues. Second, uniform conductivity is an unrealistic assumption because even within the same tissue, conductivity values can vary depending on various parameters, such as water content [7], sodium concentration [8], and anatomical structure. For example, skin conductivity is known to vary significantly from the surface layer to deeper layers [9]. The use of uniform conductivity values may provide a reasonable approximation and is widely used in dosimetry studies; however, it is still unrealistic, especially within tissue border regions [10]. Third, electrical conductivity values are typically derived from measurements presented in literature (e.g., [11]), which makes it difficult to personalize such values based on

Manuscript received December 19, 2019; accepted January 23, 2020. Date of publication January 27, 2020; date of current version June 30, 2020. This work was supported by the Ministry of Internal Affairs and Communications, Japan. *(Corresponding author: Essam A. Rashed.)*

Essam A. Rashed is with the Department of Electrical and Mechanical Engineering, Nagoya Institute of Technology, Nagoya 466-8555, Japan, and also with the Department of Mathematics, Faculty of Science, Suez Canal University, Ismailia 41522, Egypt (e-mail: essam.rashed@nitech.ac.jp).

Jose Gomez-Tames and Akimasa Hirata are with the Department of Electrical and Mechanical Engineering, Nagoya Institute of Technology, Nagoya 466-8555, Japan.

This article has supplementary downloadable material available at http://ieeexplore.ieee.org, provided by the author.

Color versions of one or more of the figures in this article are available online at http://ieeexplore.ieee.org.

Digital Object Identifier 10.1109/TMI.2020.2969682

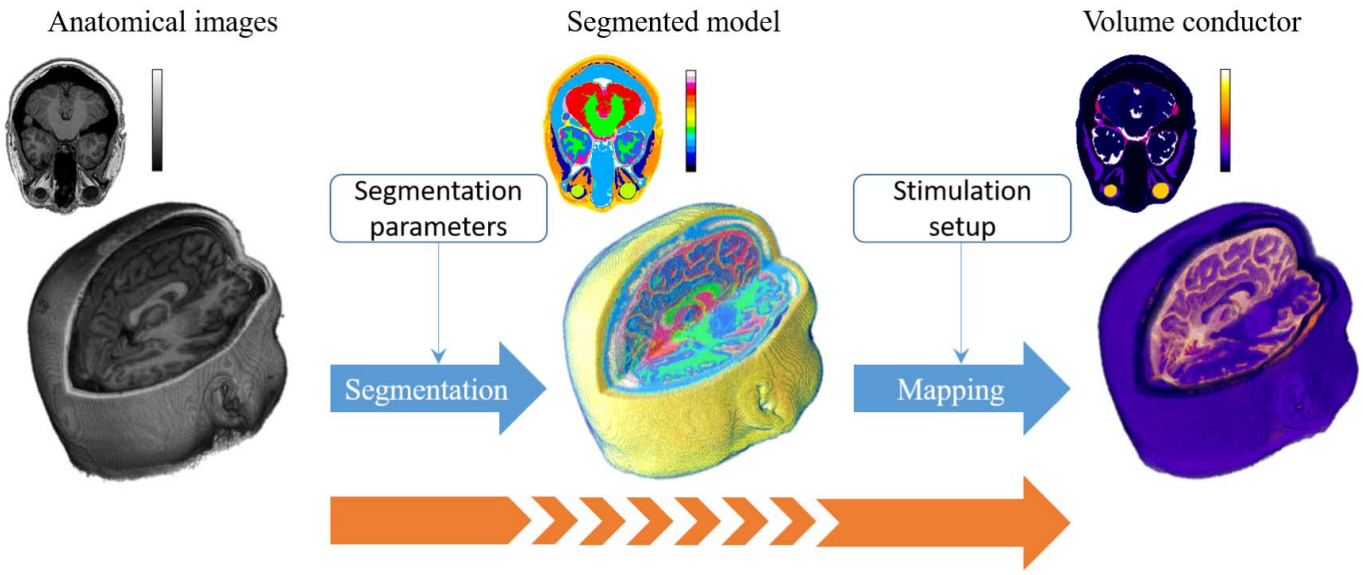


Fig. 1. Standard pipeline for the generation of volume conductor models with uniform conductivity based on anatomical images for dosimetry computations. Orange arrows indicate the contributions of this study where segmentation is not required, and non-uniform conductivity map is estimated.

measurement conditions, measurement methods, temperature, subject age, etc. [12], [13].

In our previous study, we developed an efficient deep learning architecture called ForkNet for the fast and efficient segmentation of several human head tissues [14], [15]. ForkNet can provide high-quality segmentation results that fit the pipeline presented in Fig. 1. However, there are some limitations with regard to the use of uniform conductivity assumptions for each tissue, which are also used in similar frameworks. To avoid potential errors caused by segmentation faults, several methods have been proposed to estimate the electrical properties based on anatomical images (mainly MRI) [16]–[21]. The water content calculated from T1-weighed MRI scans is modeled by a monotonic function to estimate the conductivity of major brain tissues [7]. However, such methods utilize data that is strictly limited to brain tissues. Magnetic resonance electrical impedance tomography (MREIT) was presented as a useful approach for estimating brain conductivity [22]–[24], but it is also strictly limited to brain tissues. A recent review of the methods used to estimate electrical conductivity based on MRI can be found in [25].

Deep learning has become a standard machine learning technique for various data mapping and labeling problems [26]. In particular, convolutional neural networks (CNNs) are now the leading tool for image processing and recognition. This success motivated us to investigate deep learning approaches to estimate the electric conductivity based on MRI for electromagnetic dosimetry computations and other applications.

In this paper, we propose a method for the automatic generation of volume conductor models without the segmentation of complicated head tissues. To the best of our knowledge, this paper is the first to present a method for the automatic estimation of non-uniform electric conductivity in human head models based on deep learning. The proposed method maps T1- and T2-weighted MRI scans to potential electrical conductivity values.

## II. Uniform Versus Non-Uniform Conductivity

In non-invasive electrostimulation, the simulated distributions of electric fields in the brain can be used to estimate the effects of stimulation sessions [27]. Simulation studies based on volume conductor models with finite-element or finite-difference methods are commonly used to solve Maxwell's equation. Therefore, accurate electrical conductivity predictions for different tissues in the head are required to derive precise maps of the electric field distributions in the brain. However, the estimation of accurate conductivity values is difficult because it requires reliable measurements from live homogeneous tissues. It has become a common practice in this field to use uniform conductivity values within consistent segmented tissues.

Although uniform conductivity for each tissue is widely used, it has certain limitations. To demonstrate the difference between uniform and non-uniform conductivity, we will present a single slice of two electrical conductivity maps, where one was generated using uniform conductivity (computed using the method in [28]) and the other was generated using non-uniform conductivity (computed using the method presented in this paper). The differences in conductivity values are summarized by the profile plots in Fig. 2. Uniform conductivity produces sharp edges that indicate sudden changes in conductivity values at the borders, whereas non-uniform conductivity produces much smoother results. This shows that non-uniform profiles can be interpreted as Gaussian convolutions of uniform profiles. From a computational complexity perspective, using uniform conductivity seems to be straightforward because it simply requires segmentation of anatomical images, after which each tissue can be assigned a single conductivity value. However, it is expected that segmentation

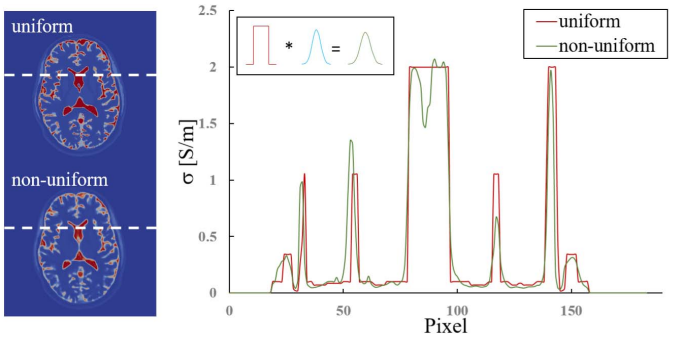


Fig. 2. Example of the differences between uniform and non-uniform electrical conductivity estimation. Sample slices are presented on the left, and the profiles of the white dashed lines are plotted on the right.

errors could have a significant influence on electric field maps, especially at the border regions between tissues with similar anatomical gray values and different conductivity measurements (e.g., muscle and gray matter (GM) or cerebrospinal fluid (CSF) and air). In such cases, segmentation errors are likely to generate relatively large errors in conductivity values. Furthermore, sudden changes in conductivity values at the border regions can produce staircase artifacts in the electric field maps. Averaging techniques and the inclusion of specific percentile values are common post-processing techniques for avoiding such artifacts [29], [30]. In contrast, non-uniform conductivity represents a more personalized approach because the conductivity at each discrete point (voxel) is assumed to be independent. The estimation of non-uniform conductivity using MRI was first proposed based on the estimation of the radio frequency penetration of MRI [31]. Recently, the electrical conductivity of brain tissues has been estimated using B1 maps from 7T MRI [32]. Almost all approaches to non-uniform conductivity estimation are based on highly sophisticated imaging modalities that place additional burdens on patients. In this study, we aimed to develop a simple and effective method to estimate the electrical conductivity using standard imaging modalities, such as T1- and T2-weighted MRI.

## III. Materials and Methods

### A. Data and Preprocessing

A set of freely available T1- and T2-weighted MRI scans containing $256^3$ voxels with a uniform voxel size of 1.0 $mm^3$ was utilized in this study.[1] The semi-automatic method presented in [28] was used to segment MRI scans from 18 subjects into different tissues, such as skin, muscle, fat, bone (cortical), bone (cancellous), dura, blood, CSF, GM, white matter (WM), cerebellum, vitreous humor, and mucous tissue. The dataset was split arbitrarily into 10 subjects for training and 8 subjects for testing. The number of subjects required for training was computed in our previous study, and we determined that 10 to 15 subjects are sufficient for stable training [14]. A bias correction is implemented for both T1 and T2 MRI [28]. Generally, in MRI brain imaging, the acquired

[1] http://hdl.handle.net/1926/1687

TABLE I
Human Tissue Conductivity Values [S/m] for (A) the Cole-Cole Model and (B) Typical Values From Computational Studies [33]

| Tissue | Conductivity $\sigma_n$ | | Tissue | Conductivity $\sigma_n$ | |
|---|---|---|---|---|---|
| | A | B | | A | B |
| Blood | 0.700 | 0.700 | GM | 0.100 | 0.276 |
| Bone (canc.) | 0.080 | 0.025 | Mucous tissue | 0.070 | 0.070 |
| Bone (cort.) | 0.020 | 0.007 | Muscle | 0.340 | 0.400 |
| Cerebellum | 0.130 | 0.276 | Skin | 0.100 | 0.456 |
| CSF | 2.000 | 1.654 | V. Humor | 1.500 | 1.500 |
| Dura | 0.500 | 0.500 | WM | 0.070 | 0.126 |
| Fat | 0.040 | 0.040 | | | |

volume provides anatomical structures down to the nose tip, while the remaining head region (from the nose tip down to the neck) is not commonly available. Therefore, the study in [28] suggested adding an artificial structure, which arbitrarily represents the missing head region, to the segmented head models. This process is important for electromagnetic studies that consider deep penetration of the electric field for targeting deep brain regions in transcranial magnetic simulation (TMS). Hence, there is some data inconsistency between the MRI images and the segmented models in terms of the neck regions (presented in the segmented models but not in the original MRI).

Segmented models are assigned to isotropic uniform tissue conductivity values using a fourth-order Cole-Cole model with a frequency of 10 kHz for TMS applications, as reported in [11]. These values are used as the conductivity measured over 10 kHz is more accurate [9] when considering the operating frequency of TMS devices [34]. The uniform conductivity values are listed in Table I (A). Moreover, an additional set of conductivity values, which represent the common values from computational studies, is also used and is listed in Table I (B). MRI scans are normalized individually in such a way that they have zero mean and unit variance, followed by scaling in the range of [0, 1]. The corresponding uniform volume conductor is scaled to the range of $[0, 1-\tau]$, where $\tau$ is a small value parameter (here, $\tau = 0.1$).

### B. Network Architecture Design

The proposed network architecture, which is called a conductivity network (CondNet), is a multitask end-to-end mapping architecture that can generally connect $U$ anatomical images to $V$ volume conductors. A simple example is presented in Fig. 3 with $U = 2$, $V = 1$, and network depth $I = 6$. The feature size for each layer is detailed in Table II. The design of CondNet is based on individual encoder tracks from several convolutional operations aimed at extracting features from anatomical images. The decoder tracks assigned to volume conductors are generated through a series of convolutional and deconvolutional operations with feedback features (skip connections) from all the encoder tracks. As detailed in Table II, the convolutional kernels ($R_{u,i}$, $S_{v,i}$, and $T_{v,i}$) can be customized to fit the feature selection and anatomical textures in different network layers. Considering $M^1, M^2, \ldots, M^U$ are the network normalized input volumes,

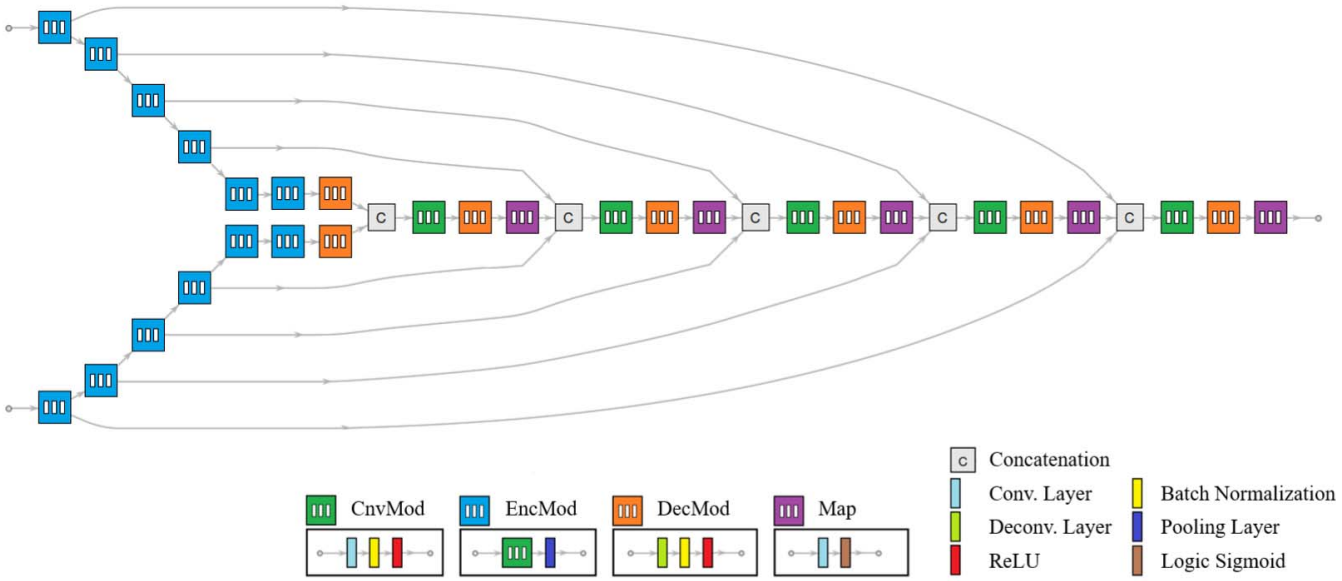


Fig. 3. Architecture of the proposed CondNet with layer identification keys. This architecture consists of two inputs ($U = 2$) and a single output ($V = 1$) with a depth of $I = 6$. Detailed feature variables for each layer are listed in Table II.

TABLE II
DETAILED ARCHITECTURE OF CONDNET (SHOWN IN FIG. 3) WITH $U$ INPUTS, $V$ OUTPUTS, AND A DEPTH OF $I$. THE CONVOLUTION KERNELS $R$, $S$, AND $T$ CAN BE CUSTOMIZED INDIVIDUALLY

| Module | Layer | Output size | Kernel | Label |
|---|---|---|---|---|
| $\text{Input}_u$<br>$u : 1 \to U$ | | $[2^8]^2$ | | |
| $\text{EncMod}_{u,i}$<br>$u : 1 \to U$<br>$i : 1 \to I$ | Convolution<br>BN & ReLU<br>Pooling (Max) | $2^{(i+1)} \times [2^{(8-i)}]^2$<br>$2^{(i+1)} \times [2^{(8-i)}]^2$<br>$2^{(i+1)} \times [2^{(7-i)}]^2$ | $2^{(i+1)} \times [R_{u,i}]^2$ | |
| Hub | Concatenation | $U \times 2^I \times [2^{(9-I)}]^2$ | | C |
| $\text{DecMod}_{v,i}$<br>$v : 1 \to V$<br>$i : (I-1) \to 1$ | Deconvolution<br>BN & ReLU | $2^{(i+1)} \times [2^{(9-i)}]^2$<br>$2^{(i+1)} \times [2^{(9-i)}]^2$ | $2^{(9-i)}$ ×2×2 | |
| $\text{CnvMod}_{v,i}$<br>$v : 1 \to V$<br>$i : (I-1) \to 1$ | Convolution<br>BN & ReLU | $2^{(i+2)} \times [2^{(8-i)}]^2$<br>$2^{(i+2)} \times [2^{(8-i)}]^2$ | $2^{(8-i)} \times [S_{v,i}]^2$ | |
| $\text{Map}_{v,i}$<br>$v = 1 \to V$<br>$i : (I-1) \to 1$ | Convolution<br>Sigmoid (Log) | $2^i \times [2^{(9-i)}]^2$<br>$\begin{cases} 2^i \times [2^{(9-i)}]^2 & i > 1 \\ [2^8]^2 & i = 1 \end{cases}$ | $2^{(9-i)} \times [T_{v,i}]^2$ | |
| $\text{Concat}_{v,i}$<br>$v : 1 \to V$<br>$i = (I-2) \to 1$ | Concatenation | $(U+1) \times 2^{(i+2)} \times [2^{(8-i)}]^2$ | | C |
| $\text{Output}_v$<br>$v = 1 \to V$ | | $[2^8]^2$ | | |

each of which has $K$ slices, and the output of the CondNet is computed as follows:

$$\{L_k^1, L_k^2, \ldots, L_k^V\} = \text{CondNet}(M_k^1, M_k^2, \ldots, M_k^U), \quad \forall k, \tag{1}$$

where $M_k^u$ is an anatomical slice from input image $u$ and $L_k^v$ is the corresponding slice from the normalized volume conductor $L^v$. Considering different slicing directions, the average normalized volume conductor is computed as the mean value obtained from different orientations as follows:

$$L_*^v = \frac{1}{3}(L_a^v + L_s^v + L_c^v), \forall v, \tag{2}$$

where $L_a$, $L_s$, and $L_c$ are normalized volume conductors computed in the axial, sagittal, and coronal directions, respectively. Finally, a standard volume conductor is computed as follows:

$$C^v = \frac{\max_n(\sigma_n^v)}{1-\tau} L_*^v, \forall n, v, \tag{3}$$

where $\sigma_n^v$ is the electrical conductivity value assigned to tissue $n$ of volume conductor $v$.

### C. Electromagnetic Simulation

The induced scalar potential $\psi$ in the volume head conductor is defined by the following equation:

$$\nabla.\sigma\nabla\psi = -\nabla.\sigma\frac{dA}{dt}, \tag{4}$$

where $A$ denotes the magnetic vector potential of the applied (external) magnetic field. The induced electric field is calculated as

$$E = -\nabla\psi - \frac{dA}{dt}. \tag{5}$$

At intermediate frequencies, such as those in TMS applications, this formulation is valid if the electric and external magnetic fields are decoupled. Additionally, the conduction currents are at least one order of magnitude greater than the displacement currents, which means that only tissue conductivity is considered while permittivity is neglected [35], [36]. Equation (4) is solved numerically by utilizing a scalar potential finite difference [36], [37] based on a multi-grid method with successive over-relaxation [38]. For comparison, we consider an isotropic uniform tissue conductivity based on a fourth-order Cole-Cole model with a frequency of 10 kHz [11]. Additionally, we consider other conductivity values that were used in previous studies as alternative values representing isotropic uniform conductivity. These values are listed in Table I (B) [33]. Our computer simulation considered TMS using a figure-eight coil located above the scalp at position C3 (10-10 electroencephalogram international system) to target the hand motor area. The TMS coil was modeled using a thin-wire approximation with outer and inner diameters of 9.7 and 4.7 cm, respectively. The coil current was set equal to the maximum stimulation output of the TMS device.

## IV. Results

### A. Conductivity Estimation

The proposed method was implemented using a workstation with four Intel (R) Xeon CPUs running at 3.60 GHz, 128 GB of memory, and three NIVIDIA GeForce GTX 1080 GPUs. The CondNet with $U = 2$, $V = 1$, and $I = 6$, which is shown in Fig. 3, was implemented using Wolfram Mathematica[2] (R) ver. 12.0. The convolution kernels were set as follows: $R_{u,i} = 3$ and $S_{v,i} = T_{v,i} = 5$. We considered the conductivity values listed in Table I (A) as true values for the training set. A set of 10 subjects was used to train three networks corresponding to different slicing directions. All slices were randomly shuffled and split with a ratio of 9:1 for training and validation, respectively. We considered cross-entropy loss function mapping, which was minimized using the ADAM algorithm [39]. Training was conducted over 50 epochs with a batch size of four. A single training session was completed in less than 9 min for each slicing direction. The plot in Fig. 4 illustrates loss function convergence. It can be seen that

[2]Wolfram Research, Inc., Champaign, IL, 2019

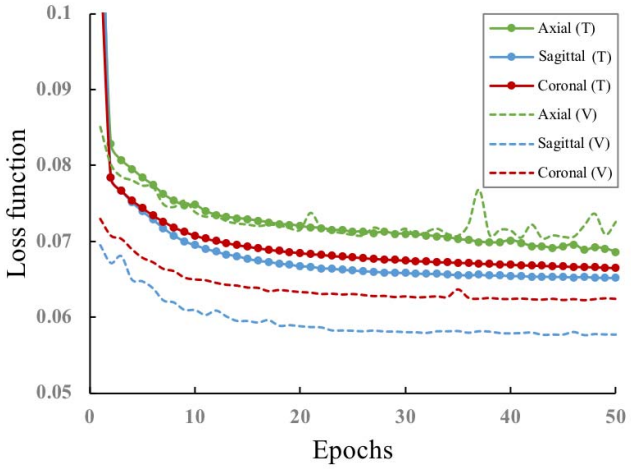


Fig. 4. Loss functions for training (T) and validation (V) for different slicing directions.

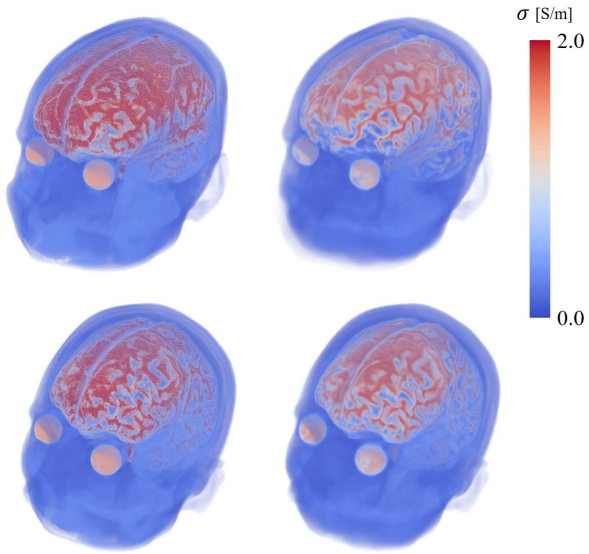


Fig. 5. The models on the left are volume conductors with uniform conductivity values computed using semi-automatic methods. The models on the right are volume conductors with non-uniform conductivity values computed using CondNet. The top models are (case01019) and the bottom models are (case01025). Two-dimensional slices with the corresponding MRI anatomies for (case01019) are presented in Fig. 6.

validation in the axial direction performs differently compared to the other two directions. This behavior is expected because the ground-truth segmented models used for training the axial network include some features that were manually added to the neck region, which has no corresponding anatomy in the MRI scans. The remaining eight subjects were used for evaluation. A volume render of two subjects is presented in Fig. 5, and a detailed example of one subject (case01019) is presented in Fig. 6.

From these results, it can be seen that CondNet is able to predict the potential conductivity within a small fluctuation range around the uniform values. The distribution of conductivity values of the CondNet-generated volume conductors exhibits more realistic patterns with smooth transitions at the tissue boundaries. Furthermore, there are some regions where

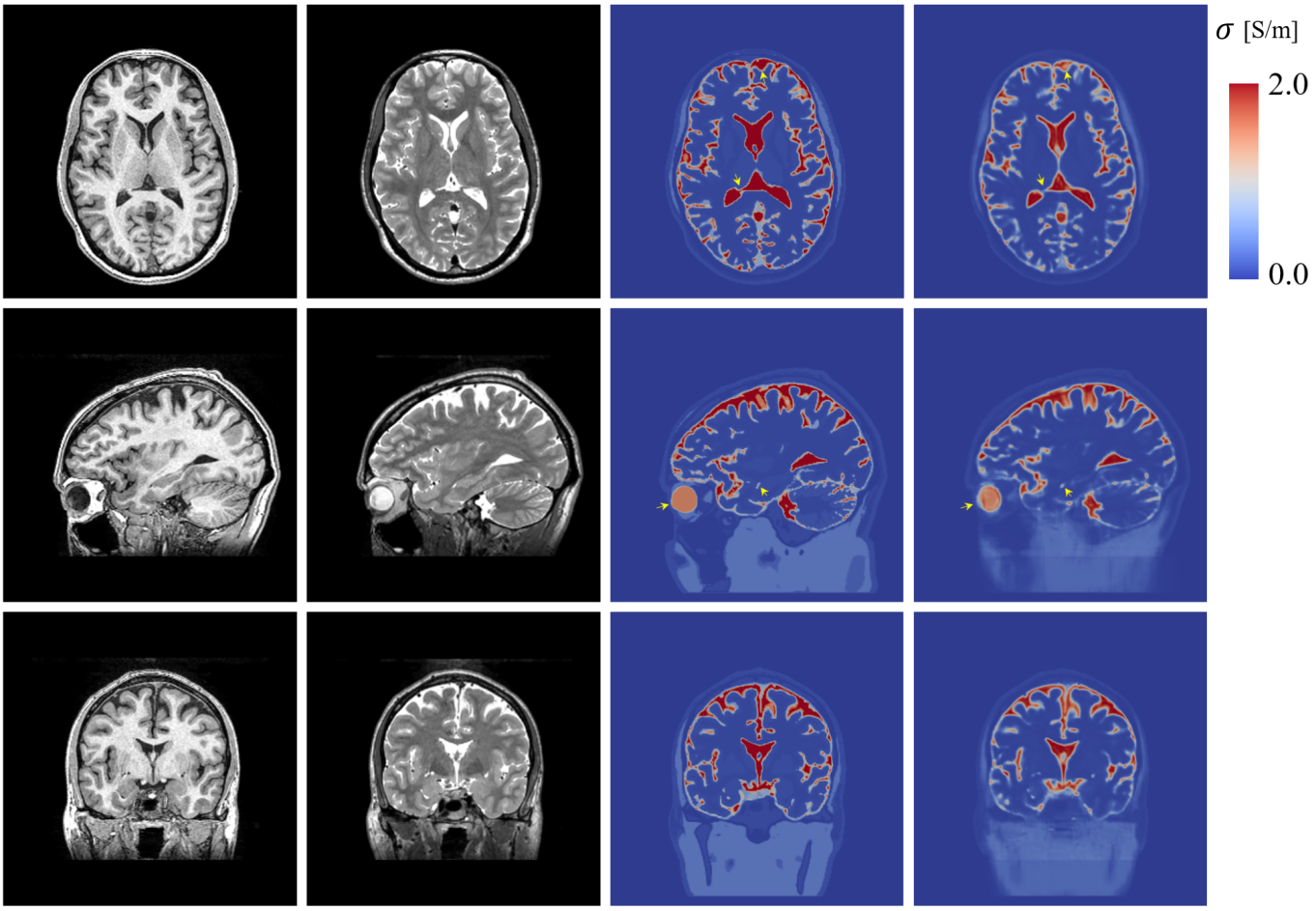


Fig. 6. From left to right: T1-weighted MRI, T2-weighted MRI, uniform conductivity maps (semi-automatic methods), and non-uniform conductivity maps (CondNet). From top to bottom: axial, sagittal, and coronal slices. Yellow arrows indicate regions in which the non-uniform conductivity values match the corresponding anatomy more closely. Regions corresponding to the neck were computed arbitrarily in CondNet images because the corresponding anatomy is unavailable. The central horizontal profiles are shown in Fig. 7.

the CondNet-generated volume conductors closely match the corresponding anatomy (Fig. 6). For example, it can be seen that the conductivity values within the eye lens are estimated with lower values compared to the surrounding vitreous humor. It is worth noting that the segmented models used for training do not contain information regarding eye lens conductivity as it is intentionally ignored and not segmented. However, when a relatively large anatomical information is missing, the CondNet conductivity values are somewhat arbitrary. This can be clearly observed in the lower neck regions of the conductivity maps presented in Fig. 6, where the corresponding neck in the uniform volume conductor is more rigid.

To demonstrate how the estimated non-uniform conductivity values are distributed at a small neighborhood scale, we compared the estimated conductivity values with standard uniform values. Seven regions of interest (ROIs) were selected from the central axial slice of (case01017) such that they contained homogeneous tissues based on the corresponding segmented model. ROIs were selected to represent samples of WM, GM, fat, bone (canc.), bone (cort.), muscle, and CSF. Both uniform and non-uniform values within limited neighborhoods are presented in Fig. 8. These results demonstrate excellent consistency when considering the variability of water content in human tissues. For example, the water contents of WM and GM in adults are known to vary from 68% to 77% and 84% to 86%, respectively [40]. Additionally, a wide range of conductivity values for different head tissues was presented in [6].

In another experiment, the network architecture was altered such that $V = 2$ (i.e., two conductivity maps were estimated simultaneously). This experiment aimed to estimate two different volume conductors based on different tissue conductivity values in a single shot. The network was trained using conductivity values obtained from the Cole-Cole model (A) and the typical computational values (B) in Table I. The remaining CondNet parameters were similar to the previous experiment. The testing results and the corresponding non-uniform models for (case01025) are presented in Fig. 9. It can be seen that the CondNet-generated volume conductors exhibit a similar distribution of electrical conductivity values. In some regions, where differences can be observed, the CondNet results exhibit closer matches to the corresponding anatomical structures.

### B. TMS Simulation

A TMS-induced electric field was used to investigate the effects of the proposed approach. Electric fields were computed using the original uniform head model and

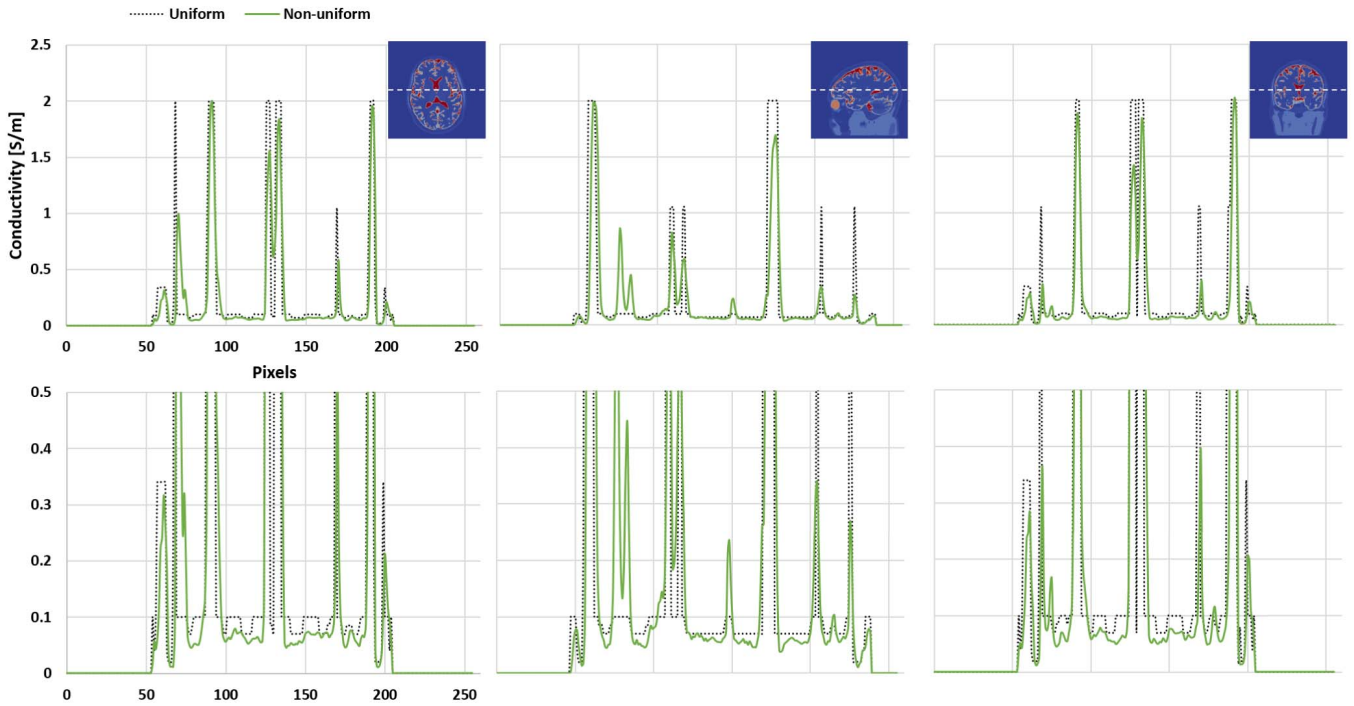


Fig. 7. From left to right: central horizontal profiles of conductivity maps shown in Fig. 6 for axial, sagittal, and coronal slices. Below are the profiles with compressed scale to magnify the variations in low-conductivity tissues.

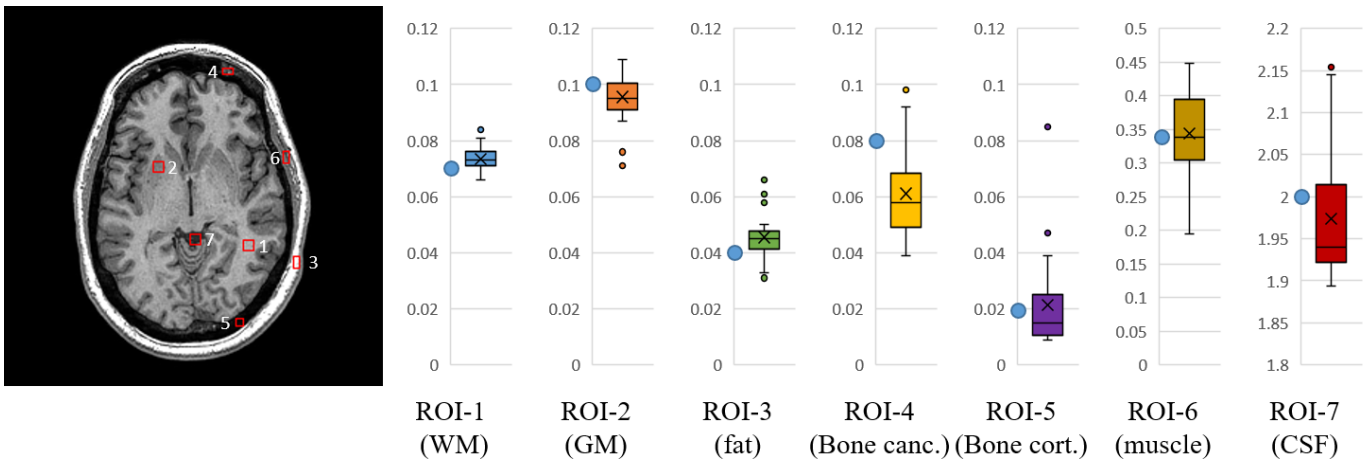


Fig. 8. ROI positions and labels in the central axial slice of (case01017) are presented on the left. The right side of the figure presents a boxplot of the conductivity values with uniform (blue circle over the y axis) and non-uniform (box) volume conductors. The ROIs represent WM, GM, fat, bone (canc.), bone (cort.), muscle, and CSF in order.

network-generated conductivity models for eight subjects. The TMS coil was placed at position C3 to target the hand motor area. Figure 10 presents the electric fields for the cortical surface and a representative sagittal plane. Additionally, the differences between the electric fields in the hand motor area (target region) and sagittal plane are highlighted. The field distributions on the cortical surfaces are similar, but the CSF content variations could affect the spread and intensity because the network-generated model exhibits graded conductivity values between boundaries. For some subjects, the differences are more significant depending on large discrepancies in the conductivity distributions, particularly for the target region. However, the differences are still within reasonable ranges considering the subject variability.

To highlight the difference between electric field distributions, magnified regions of the sagittal slices of four subjects are presented in Fig. 11. The global distributions of the electric fields are consistent, but the models generated with non-uniform conductivity exhibit homogeneous patterns with fewer staircase artifacts. The global error (GE) is defined as follows:

$$GE = \frac{1}{\max_{i\in\Omega}(E_i, \hat{E}_i)} \times \frac{\sum_{i=1}^{I} |E_i - \hat{E}_i|}{I} \times 100\%, \quad (6)$$

where $E$ and $\hat{E}$ are the internal electric fields computed using uniform and non-uniform conductivity, respectively. The computed difference values are listed in Table III to quantify the electric field distributions in different regions. In the case of

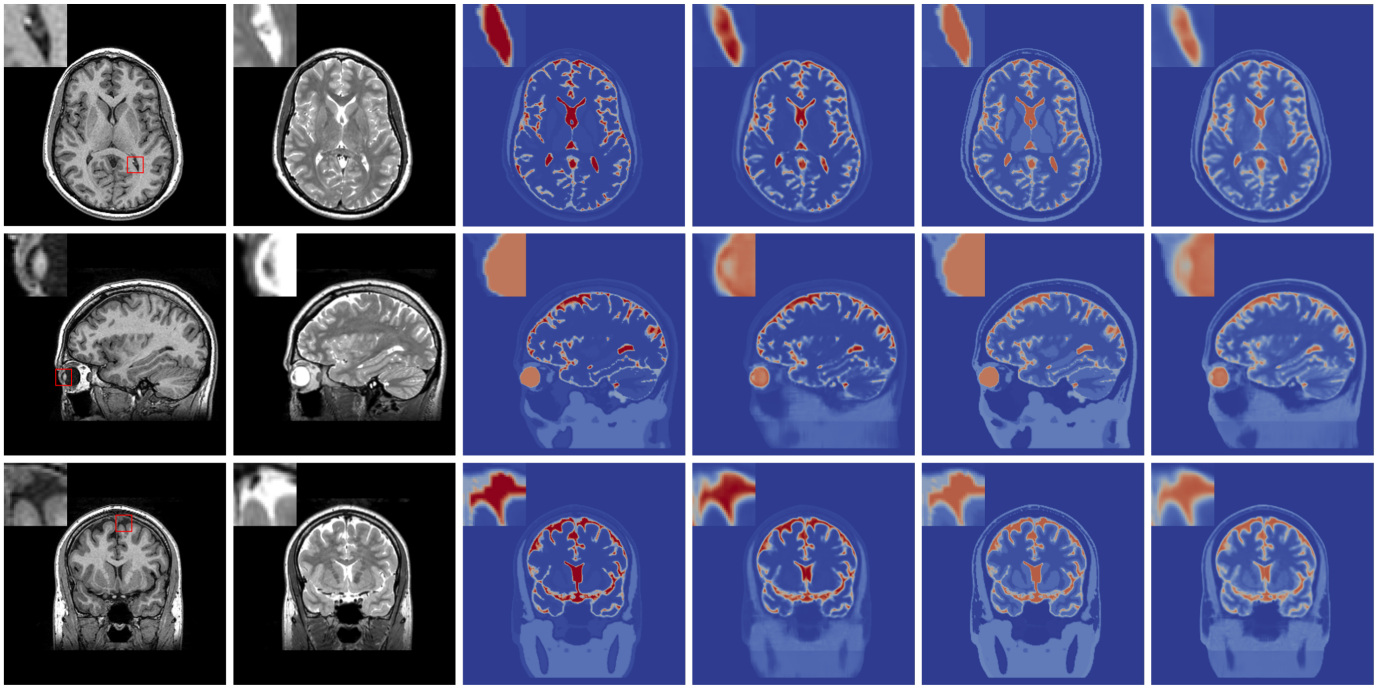

Fig. 9. Two sets of electrical conductivity maps corresponding to the values listed in Table I (A) and (B). The maps were generated using CondNet and compared with uniform conductivity maps. From left to right: T1-weighted MRI, T2-weighted MRI, uniform (A), non-uniform (A), uniform (B), and non-uniform (B) conductivity maps. From top to bottom: axial, sagittal, and coronal slices. The ROIs labeled in the leftmost column are magnified in the top-left corner of each image. It is clear from these ROIs that non-uniform conductivity maps provide a better representation of real anatomical structures.

TABLE III
GE OF THE ELECTRIC FIELDS IN DIFFERENT GROUPS OF HEAD TISSUES

| # | Subject | GE [%] (mean±std) | | | |
|---|---|---|---|---|---|
| | | Motor Area (Hand knob) | Brain | Non-Brain | Head |
| 1 | case01017 | 6.0±4.6 | 0.7±1.2 | 0.9±1.6 | 0.3±1.0 |
| 2 | case01019 | 5.5±4.2 | 0.8±1.4 | 1.1±2.3 | 0.4±1.2 |
| 3 | case01025 | 2.9±2.9 | 0.7±1.2 | 1.0±1.9 | 0.3±1.1 |
| 4 | case01028 | 6.0±4.2 | 0.8±1.4 | 0.8±1.7 | 0.3±1.0 |
| 5 | case01034 | 7.9±6.0 | 0.7±1.2 | 1.0±1.9 | 0.4±1.2 |
| 6 | case01039 | 7.7±5.4 | 0.7±1.3 | 0.9±1.8 | 0.3±1.0 |
| 7 | case01042 | 11.8±9.9 | 0.7±1.0 | 1.1±1.9 | 0.3±0.9 |
| 8 | case01045 | 6.0±4.5 | 0.6±1.1 | 0.9±1.8 | 0.3±1.0 |
| | average | 6.725 | 0.7125 | 0.9625 | 0.325 |

TABLE IV
SCANNER AND SUBJECT DETAILS FOR SELECTED SAMPLES FROM THE TCGA DATASET USED FOR GENERALITY VALIDATION STUDY

| Subject ID | TCGA-02-0006 | TCGA-14-1794 | TCGA-19-0963 |
|---|---|---|---|
| **Manufacturer** | GE Med. Sys. | Philips Med. Sys. | Siemens |
| **Model** | Genesis | Intra | Symphony |
| **Gender** | F | M | M |
| **Age** | 56 | N/A | 61 |
| **Image size** | 256×256 | 512×512 | 256×224 |
| **Pixel Spacing (mm)** | 0.781×0.781 | 0.449×0.449 | 0.898×0.898 |
| **Magnetic Field (T)** | 1.5 | 1.5 | 1.5 |
| **T1 Series** | AX T1 | AX T1 PRE | MRHG T1 AX |
| **T2 Series** | AX T2 FSE | T2 GRASE | MRHG T2 AX |

the hand motor area, the ROI was set to the hand knob region on the standard brain template centered on MNI (-42,-13,66) with a radius of 5 mm, which corresponds to the vicinity of the TMS hotspot for the abductor pollicis brevis muscle. The standard brain template ROI was projected onto each individual head model to obtain a corresponding ROI for each individual [41]. The error is greatest in the hand motor area, where stronger electric fields are present, and the differences between models may be more significant depending on the high conductivity contrast between tissues. In the brain, non-brain, and whole head regions, the global error is attenuated (conductivity contrast is smaller within the brain and other tissues).

## V. GENERALITY OF CONDNET

MRI is a highly biased imaging modality with relatively high-intensity variability within inter- and intra-scanner evaluations. Therefore, a general automatic estimation that can be used in different scanners is highly challenging and requires several normalization and calibration pre-processing steps to achieve high performance. In deep learning, this problem can be efficiently handled by employing transfer learning [42]. However, the generality of the proposed architecture is investigated through estimation of the conductivity maps of MRI images obtained from different scanners without conducting further training. The evaluation data are obtained from The Cancer Genome Atlas (TCGA), which is publicly available in The Cancer Imaging Archive (TCIA).[3] A sample of three subjects demonstrating T1/T2 MRI acquired using different scanner manufacturer in different institutes are shown in Fig. 12. Summarized information of the selected sample is shown in Table IV, while full data description is available online. As the images are presented in different resolutions,

[3]https://www.cancerimagingarchive.net/

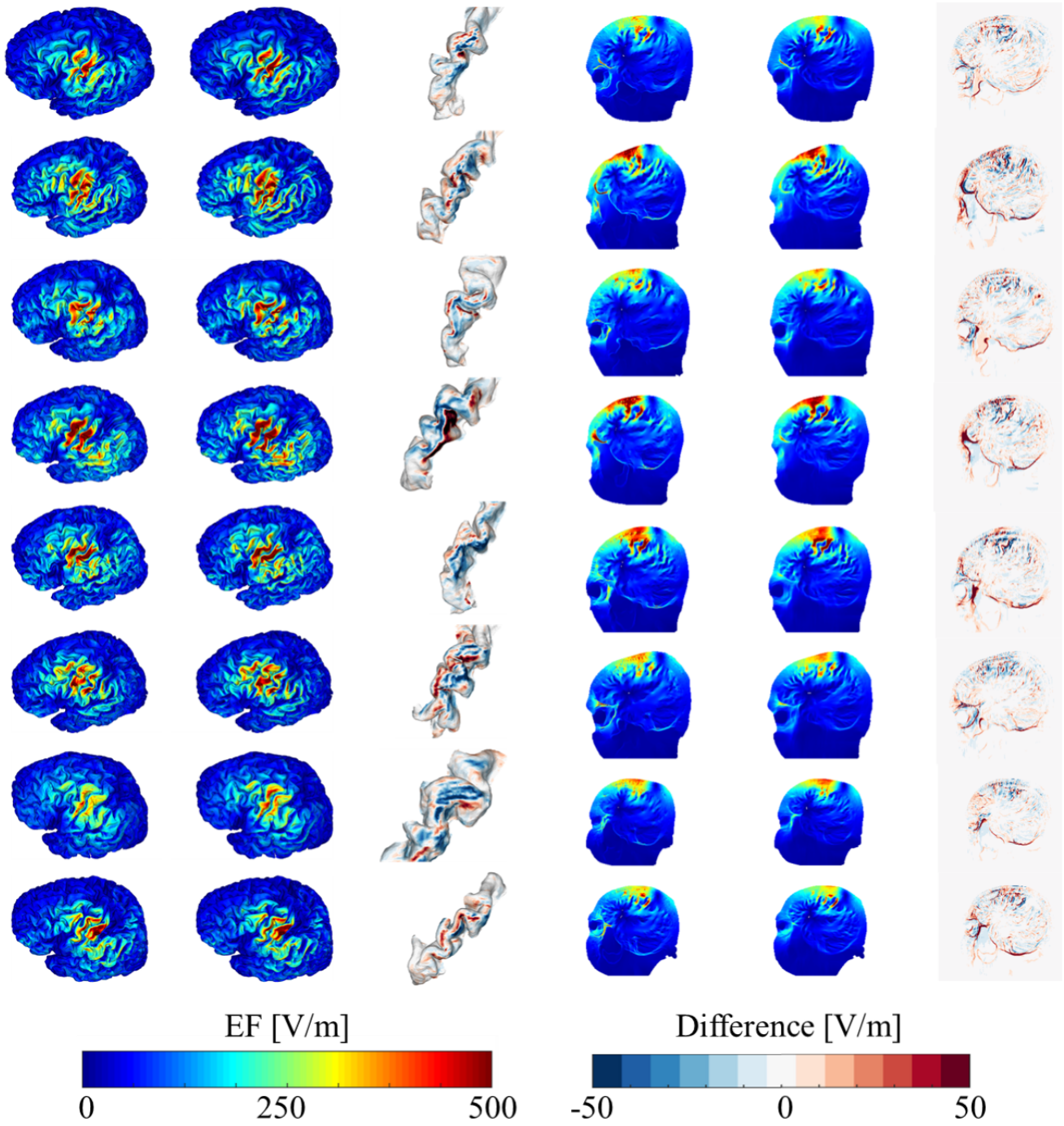


Fig. 10. Electric field distributions. The subjects listed in Table III are presented in order from top to bottom. The first two columns are the electric field maps for the brains using uniform ($E$) and non-uniform ($\hat{E}$) conductivity values, respectively, and the third column represents the error within the hand motor area. The fourth and fifth columns are the electric field maps for the head (sagittal section) with uniform and non-uniform conductivity values. The sagittal section error ($E$ - $\hat{E}$) is presented in the rightmost column.

a re-sampling process is employed to convert the image resolution to 1.0 $mm^3$. To demonstrate the variability in T1/T2 gray values and the corresponding estimated conductivity using CondNet, eight ROIs are selected in each subject to represent different anatomical tissues. The estimated conductivity values within the labeled ROIs are shown in Fig. 13 and summarized in Table V. Considering the large variation in the original T1/T2 gray values, the estimated conductivity values are within a reasonable consistency range. Additional study considering the estimation of electrical conductivity of brain tumor is included as supplementary material.

## VI. Discussion

Personalized TMS utilizing the current paradigm is a time-consuming process that is difficult to implement clinically. In a recent study, it was reported that TMS-induced electric fields have weak sensitivity to conductivity variations [43]. Therefore, there is a frame in which non-uniform

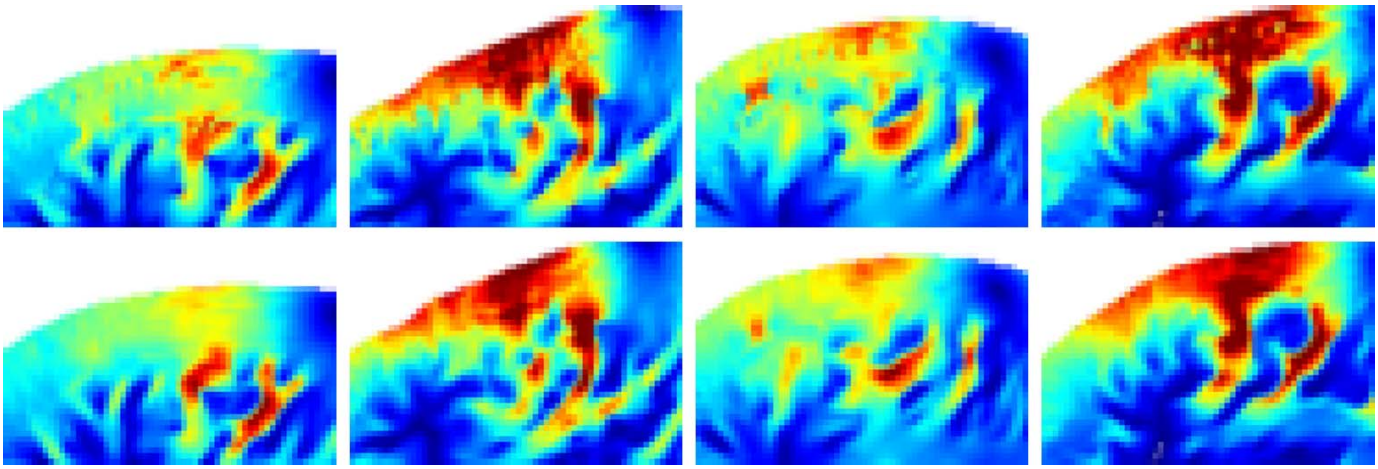

Fig. 11. Magnified cortical regions presented in Fig. 10. From left to right are subjects case01017, 19, 25, and 28. The top and bottom rows are the electric field maps corresponding to uniform and non-uniform conductivity values, respectively. Highly consistent distributions of electric fields can be observed, but the maps generated using non-uniform conductivity values largely eliminate the staircase artifacts.

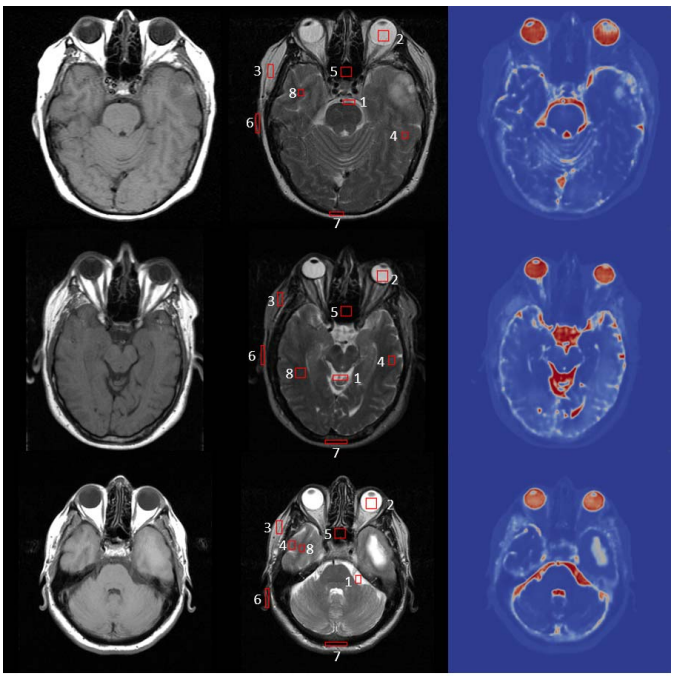

Fig. 12. From left to right: T1-, T2-weighted MRI, and CondNet non-uniform conductivity maps. From top to bottom: subjects TCGA-02-0006, TCGA-14-1794, and TCGA-19-0963. The labeled ROIs represent CSF, V. humor, fat, GM, mucous tissue, skin, bone cort., and WM, in order.

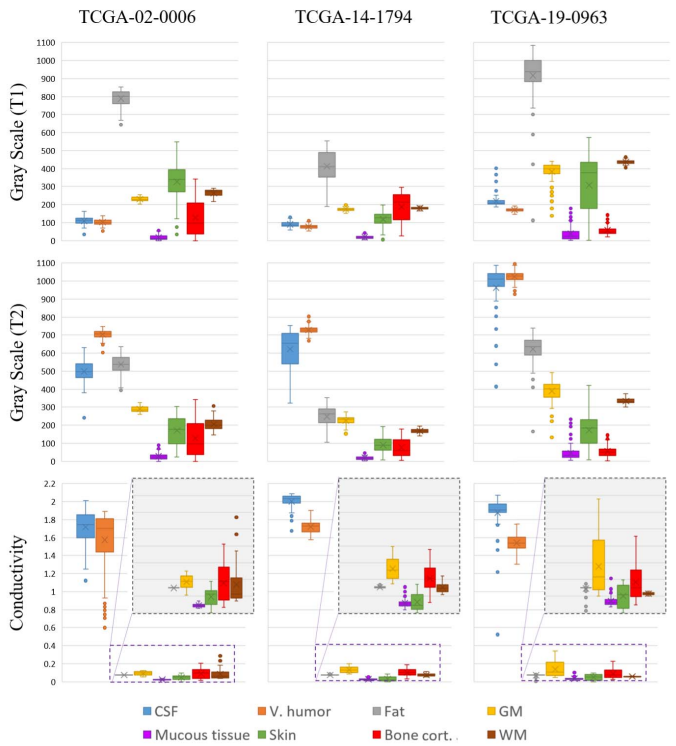


Fig. 13. Box plot demonstrating the distribution of gray values in T1 and T2 MRI, and the corresponding estimated conductivity within regions labeled in Fig. 12. The conductivity plots of the later six tissues are magnified in a compressed scale for clarity.

conductivity will produce comparable results. The only way to compute accurate conductivity is through physical measurements, which is obviously unfeasible. In this study, we developed a novel CNN architecture for the estimation of non-uniform electrical conductivity in human head models based on anatomical information extracted from T1- and T2-weighted MRI scans. The developed learning-based conductivity generator network can achieve high accuracy by utilizing a limited training dataset containing only 10 subjects. This novel architecture provides several advantages. First, it does not require highly sophisticated imaging modalities and can estimate accurate conductivity values based on standard MRI scans. Second, CondNet provides conductivity maps that are highly consistent with the anatomical structures. For example, the conductivity of eye lens that is not considered in training is estimated with a value ranging between 0.31 and 0.55 (reference true value is 0.34 S/m [11]). Third, employing CondNet can facilitate precision medicine in which a personalized head model can be generated in a short timeframe without the need for segmentation, which is time consuming. Furthermore, it can be extended to the estimation of head models that are suitable for different stimulation scenarios in a

TABLE V
MEAN ± SD OF THE ESTIMATED CONDUCTIVITY VALUE WITHIN ROIS MARKED IN FIG. 12

| # | Tissue | Trained | TCGA subject | | |
|---|---|---|---|---|---|
| | | | 02-0006 | 14-1794 | 19-0963 |
| 1 | CSF | 2.00 | 1.72±0.19 | 2.00±0.08 | 1.88±0.22 |
| 2 | V. humor | 1.50 | 1.57±0.31 | 1.72±0.07 | 1.54±0.10 |
| 3 | Fat | 0.04 | 0.07±0.00 | 0.08±0.00 | 0.07±0.01 |
| 4 | GM | 0.10 | 0.09±0.02 | 0.13±0.03 | 0.14±0.08 |
| 5 | Mucous | 0.07 | 0.03±0.00 | 0.03±0.01 | 0.03±0.01 |
| 6 | Skin | 0.1 | 0.05±0.03 | 0.03±0.03 | 0.05±0.03 |
| 7 | Bone (cort.) | 0.02 | 0.09±0.05 | 0.10±0.04 | 0.09±0.05 |
| 8 | WM | 0.07 | 0.08±0.06 | 0.07±0.01 | 0.06±0.00 |

single operation. Therefore, it can be used for brain stimulation planning for different clinical applications and the optimization of TMS dosing (e.g., [44]).

Head models with non-uniform conductivity maps were evaluated based on TMS simulation of the hand motor area and compared with standard head models generated via segmentation with uniform conductivity. Generally, the patterns of electric field distributions generated by the two models are very consistent. However, upon closer observation, it was determined that staircase artifacts were present in the head models with uniform conductivity, whereas the CondNet models provided a more natural and uniform distribution of electric fields. Quantitative analysis demonstrated that a relatively small difference can be achieved, which can be referred to the staircase artifacts in models with uniform conductivity values.

The CondNet estimated conductivity results has some similarity with the tissue probability maps (TPMs) method [45] with conductivity-weighted. However, most of the available tools/software for TPMs, such as SPM[4] can provide probability maps for limited number of tissues (mainly brain). In brain electrical stimulation, the conductivity values of non-brain tissues are also required. We have found that deep learning can handle this problem in an efficient way. The proposed architecture has a general form that can be extended in the future to include additional anatomical images with additional fine-tuning features, such as fiber orientations (DTI), blood vessels (venograms), and tumor activities (PET/SPECT). Additionally, it can be easily extended to generate models representing different electromagnetic properties, such as permittivity, as well as models that fit a wide range of frequencies. As shown in the results section, the proposed architecture is relatively fast in terms of both training (minutes) and testing (seconds), which should make it usable in clinical applications. It is expected that this approach will contribute to enhanced electromagnetic stimulation that can automatically estimate highly reliable conductivity values without time-consuming segmentation.

A potential limitation of CondNet is that it does not consider conductivity anisotropy. The anisotropy of non-brain tissues (e.g., skull) may affect the electric field distribution, but its inclusion is not supported [46]. The anisotropy of brain tissues is expected to affect deep brain tissues, but it is negligible for the superior parts. Therefore, the evaluation of the electric field on the cortical surface is valid. Moreover, CondNet is presented in a general form where additional information from different modalities such as diffuse tensor imaging, CT, venogram, etc., can be added in a further extended version.

[4]https://www.fil.ion.ucl.ac.uk/spm/

## VII. CONCLUSION

A novel CNN architecture was proposed for the automatic generation of human head models with non-uniform electric conductivity. The proposed CondNet was trained using uniform volume conductors, and it quickly estimated the non-uniform conductivity values of unknown subjects based on T1- and T2-weighted MRI scans. The proposed network has several merits in terms of enabling precision medicine applications for brain stimulation. First, intensive segmentation of multiple head tissues is not required, which reduces time and effort significantly compared to manual segmentation approaches. Second, as shown by the results presented in this paper, CondNet is able to estimate the conductivity values of anatomical structures that are not present in a training dataset. Third, CondNet has the ability to generate different volume conductors associated with multiple brain stimulation scenarios in a single operation. This should provide a flexible framework that can handle alternative stimulation conditions. The source code used in this study will be provided by the corresponding author upon receiving a reasonable request.

## REFERENCES

[1] W. Kainz *et al.*, "Advances in computational human phantoms and their applications in biomedical engineering—A topical review," *IEEE Trans. Radiat. Plasma Med. Sci.*, vol. 3, no. 1, pp. 1–23, 2019.
[2] T. R. Insel and B. N. Cuthbert, "Brain disorders? Precisely," *Science*, vol. 348, no. 6234, pp. 499–500, May 2015.
[3] D. Comaniciu, K. Engel, B. Georgescu, and T. Mansi, "Shaping the future through innovations: From medical imaging to precision medicine," *Med. Image Anal.*, vol. 33, pp. 19–26, Oct. 2016.
[4] E. A. Rashed, T. Sakai, J. Gomez-Tames, and A. Hirata, "Brain AI: Deep learning for brain stimulation," *IEEE Pulse*, vol. 10, no. 4, pp. 3–5, Jul. 2019.
[5] T. Wagner, A. Valero-Cabre, and A. Pascual-Leone, "Noninvasive human brain stimulation," *Annu. Rev. Biomed. Eng.*, vol. 9, pp. 527–565, Aug. 2007.
[6] H. Mccann, G. Pisano, and L. Beltrachini, "Variation in reported human head tissue electrical conductivity values," *Brain Topogr.*, vol. 32, no. 5, pp. 825–858, Sep. 2019.
[7] E. Michel, D. Hernandez, and S. Y. Lee, "Electrical conductivity and permittivity maps of brain tissues derived from water content based on T1-weighted acquisition," *Magn. Reson. Med.*, vol. 77, no. 3, pp. 1094–1103, Mar. 2017.
[8] Y. Liao, N. Lechea, A. W. Magill, W. A. Worthoff, V. Gras, and N. J. Shah, "Correlation of quantitative conductivity mapping and total tissue sodium concentration at 3T/4T," *Magn. Reson. Med.*, vol. 82, no. 4, pp. 1518–1526, Oct. 2019.
[9] K. Wake, K. Sasaki, and S. Watanabe, "Conductivities of epidermis, dermis, and subcutaneous tissue at intermediate frequencies," *Phys. Med. Biol.*, vol. 61, no. 12, pp. 4376–4389, Jun. 2016.
[10] N. Gurler and Y. Z. Ider, "Gradient-based electrical conductivity imaging using MR phase," *Magn. Reson. Med.*, vol. 77, no. 1, pp. 137–150, Jan. 2017.
[11] S. Gabriel, R. W. Lau, and C. Gabriel, "The dielectric properties of biological tissues: III. Parametric models for the dielectric spectrum of tissues," *Phys. Med. Biol.*, vol. 41, no. 11, pp. 2271–2293, Nov. 1996.
[12] J. Wang, O. Fujiwara, and S. Watanabe, "Approximation of aging effect on dielectric tissue properties for SAR assessment of mobile telephones," *IEEE Trans. Electromagn. Compat.*, vol. 48, no. 2, pp. 408–413, May 2006.
[13] A. Peyman, S. J. Holden, S. Watts, R. Perrott, and C. Gabriel, "Dielectric properties of porcine cerebrospinal tissues at microwave frequencies: *in vivo*, *in vitro* and systematic variation with age," *Phys. Med. Biol.*, vol. 52, no. 8, pp. 2229–2245, Apr. 2007.

[14] E. A. Rashed, J. Gomez-Tames, and A. Hirata, "Development of accurate human head models for personalized electromagnetic dosimetry using deep learning," *NeuroImage*, vol. 202, Nov. 2019, Art. no. 116132.

[15] E. A. Rashed, J. Gomez-Tames, and A. Hirata, "Generation of head models for brain stimulation using deep convolution networks," in *Proc. IEEE Int. Conf. Image Process. (ICIP)*, Sep. 2019, pp. 2621–2625.

[16] K. M. Ropella and D. C. Noll, "A regularized, model-based approach to phase-based conductivity mapping using MRI," *Magn. Reson. Med.*, vol. 78, no. 5, pp. 2011–2021, Nov. 2017.

[17] N. M. H. Elsaid, A. I. Nachman, W. Ma, T. P. Demonte, and M. L. G. Joy, "The impact of anisotropy on the accuracy of conductivity imaging: A quantitative validation study," *IEEE Trans. Med. Imaging*, vol. 36, no. 2, pp. 507–517, Feb. 2017.

[18] N. Hampe, M. Herrmann, T. Amthor, C. Findeklee, M. Doneva, and U. Katscher, "Dictionary-based electric properties tomography," *Magn. Reson. Med.*, vol. 81, no. 1, pp. 342–349, Jan. 2019.

[19] J. E. C. Serralles *et al.*, "Noninvasive estimation of electrical properties from magnetic resonance measurements via global Maxwell tomography and match regularization," *IEEE Trans. Biomed. Eng.*, vol. 67, no. 1, pp. 3–15, Jan. 2020.

[20] K. K. Tha *et al.*, "Noninvasive electrical conductivity measurement by MRI: A test of its validity and the electrical conductivity characteristics of glioma," *Eur. Radiol*, vol. 28, no. 1, pp. 348–355, Jan. 2018.

[21] P. Farace, R. Pontalti, L. Cristoforetti, R. Antolini, and M. Scarpa, "An automated method for mapping human tissue permittivities by MRI in hyperthermia treatment planning," *Phys. Med. Biol.*, vol. 42, no. 11, pp. 2159–2174, Nov. 1997.

[22] M. Chauhan, A. Indahlastari, A. K. Kasinadhuni, M. Schar, T. H. Mareci, and R. J. Sadleir, "Low-frequency conductivity tensor imaging of the human head *in vivo* using DT-MREIT: First study," *IEEE Trans. Med. Imag.*, vol. 37, no. 4, pp. 966–976, Apr. 2018.

[23] O. I. Kwon *et al.*, "Current density imaging during transcranial direct current stimulation using DT-MRI and MREIT: Algorithm development and numerical simulations," *IEEE Trans. Biomed. Eng.*, vol. 63, no. 1, pp. 168–175, Jan. 2016.

[24] O. I. Kwon, W. C. Jeong, S. Z. K. Sajib, H. J. Kim, and E. J. Woo, "Anisotropic conductivity tensor imaging in MREIT using directional diffusion rate of water molecules," *Phys. Med. Biol.*, vol. 59, no. 12, pp. 2955–2974, Jun. 2014.

[25] J. Liu, Y. Wang, U. Katscher, and B. He, "Electrical properties tomography based on $B_1$ maps in MRI: Principles, applications, and challenges," *IEEE Trans. Biomed. Eng.*, vol. 64, no. 11, pp. 2515–2530, 2017.

[26] Y. LeCun, Y. Bengio, and G. Hinton, "Deep learning," *Nature*, vol. 521, no. 7553, pp. 436–444, 2015.

[27] D. Balslev, W. Braet, C. Mcallister, and R. C. Miall, "Inter-individual variability in optimal current direction for transcranial magnetic stimulation of the motor cortex," *J. Neurosci. Methods*, vol. 162, nos. 1–2, pp. 309–313, May 2007.

[28] I. Laakso, S. Tanaka, S. Koyama, V. De Santis, and A. Hirata, "Inter-subject variability in electric fields of motor cortical tDCS," *Brain Stimulation*, vol. 8, no. 5, pp. 906–913, Sep. 2015.

[29] A. Hirata, Y. Takano, Y. Kamimura, and O. Fujiwara, "Effect of the averaging volume and algorithm on the *in situ* electric field for uniform electric- and magnetic-field exposures," *Phys. Med. Biol.*, vol. 55, no. 9, pp. N243–N252, 2010.

[30] J. Gomez-Tames, I. Laakso, Y. Haba, A. Hirata, D. Poljak, and K. Yamazaki, "Computational artifacts of the *in situ* electric field in anatomical models exposed to low-frequency magnetic field," *IEEE Trans. Electromagn. Compat.*, vol. 60, no. 3, pp. 589–597, Jun. 2018.

[31] E. M. Haacke, L. S. Petropoulos, E. W. Nilges, and D. H. Wu, "Extraction of conductivity and permittivity using magnetic resonance imaging," *Phys. Med. Biol.*, vol. 36, no. 6, pp. 723–734, Jun. 1991.

[32] Y. Wang, P.-F. Van De Moortele, and B. He, "Automated gradient-based electrical properties tomography in the human brain using 7 Tesla MRI," *Magn. Reson. Imag.*, vol. 63, pp. 258–266, Nov. 2019.

[33] S. Aonuma *et al.*, "A high-resolution computational localization method for transcranial magnetic stimulation mapping," *NeuroImage*, vol. 172, pp. 85–93, May 2018.

[34] J. O. Nieminen, L. M. Koponen, and R. J. Ilmoniemi, "Experimental characterization of the electric field distribution induced by TMS devices," *Brain Stimulation*, vol. 8, no. 3, pp. 582–589, May 2015.

[35] T. W. Dawson and M. Stuchly, "Analytic validation of a three-dimensional scalar-potential finite-difference code for low-frequency magnetic induction," *Appl. Comput. Electromagn. Soc. J.*, vol. 11, no. 3, pp. 72–81, 1996.

[36] A. Hirata, F. Ito, and I. Laakso, "Confirmation of quasi-static approximation in SAR evaluation for a wireless power transfer system," *Phys. Med. Biol.*, vol. 58, no. 17, pp. N241–N249, Sep. 2013.

[37] A. Hirata *et al.*, "Intercomparison of induced fields in Japanese male model for ELF magnetic field exposures: Effect of different computational methods and codes," *Radiat. Protection Dosimetry*, vol. 138, no. 3, pp. 237–244, Mar. 2010.

[38] I. Laakso and A. Hirata, "Fast multigrid-based computation of the induced electric field for transcranial magnetic stimulation," *Phys. Med. Biol.*, vol. 57, no. 23, pp. 7753–7765, Dec. 2012.

[39] D. P. Kingma and J. Ba, "Adam: A method for stochastic optimization," 2014, *arXiv:1412.6980*. [Online]. Available: https://arxiv.org/abs/1412.6980

[40] W. S. Snyder, M. J. Cook, E. S. Nasset, L. R. Karhausen, G. P. Howells, and I. H. Tipton, *Report of the Task Group on Reference Man*. New York, NY, USA: Pergamon, 1975.

[41] S. Diekhoff *et al.*, "Functional localization in the human brain: Gradient-echo, spin-echo, and arterial spin-labeling fMRI compared with neuronavigated TMS," *Hum. Brain Mapping*, vol. 32, no. 3, pp. 341–357, Mar. 2011.

[42] A. Van Opbroek, H. C. Achterberg, M. W. Vernooij, and M. De Bruijne, "Transfer learning for image segmentation by combining image weighting and kernel learning," *IEEE Trans. Med. Imag.*, vol. 38, no. 1, pp. 213–224, Jan. 2019.

[43] G. B. Saturnino, A. Thielscher, K. H. Madsen, T. R. Knösche, and K. Weise, "A principled approach to conductivity uncertainty analysis in electric field calculations," *NeuroImage*, vol. 188, pp. 821–834, Mar. 2019.

[44] J. Gomez-Tames, A. Hamasaka, I. Laakso, A. Hirata, and Y. Ugawa, "Atlas of optimal coil orientation and position for TMS: A computational study," *Brain Stimulation*, vol. 11, no. 4, pp. 839–848, Jul. 2018.

[45] J. Ashburner and K. J. Friston, "Unified segmentation," *NeuroImage*, vol. 26, no. 3, pp. 839–851, Jul. 2005.

[46] R. J. Sadleir and A. Argibay, "Modeling skull electrical properties," *Ann. Biomed. Eng.*, vol. 35, no. 10, pp. 1699–1712, Sep. 2007.